Chemical Engineering Journal 518 (2025) 164738

Contents lists available at ScienceDirect

Chemical Engineering Journal

journal homepage: www.elsevier.com/locate/cej

Vanadium dioxide - Perovskite tandem smart windows achieve full-spectrum modulation via plasmonic Fabry-Pérot engineering

Qiuyi Shi [a,1], Bowen Li [b,1], Yuwei Du [a], Sai Liu [a], Rui Zhang [a], Cancheng Jiang [a], Xin Li [a], Muhammad Fahim [a], Irum Firdous [a], Johnny C.Y. Ho [b,*], Chi Yan Tso [a,*]

[a] *School of Energy and Environment, City University of Hong Kong, Tat Chee Avenue, Kowloon Tong, Hong Kong, China*

[b] *Department of Materials Science and Engineering, City University of Hong Kong, Tat Chee Avenue, Kowloon Tong, Hong Kong, China*

ARTICLE INFO

Keywords:
Green buildings
Phase transition
Thermochromic perovskite
Smart windows
Radiative cooling

ABSTRACT

Conventional thermochromic windows are limited by their single-band modulation, which restricts their ability to simultaneously manage solar light and mid-infrared heat radiation. This study introduces a novel Full-spectrum Modulated Perovskite-based Smart Window (FMPSW) that can simultaneously regulate solar light transmittance and mid-infrared emissivity in response to thermal changes while maintaining high luminous transmittance. By integrating optical simulations with experimental validation, the optimized FMPSW design demonstrates exceptional energy-saving potential through the incorporation of Fabry-Pérot resonance and surface plasmon polaritons (SPPs). The optimized design achieves remarkable solar modulation (16 %) and emissivity modulation (33.4 %) simultaneously, with a cold-state luminous transmittance exceeding 40 %. Experimental results also show a maximum emissivity adjustment of 46 % without compromising high luminous transmittance levels. Furthermore, EnergyPlus simulations confirm the practical applicability of FMPSW, demonstrating significant energy savings across cold (Beijing), temperate (Shanghai), and sub-tropical (Hong Kong) climates. Specifically, the proposed window system achieves a 22.66 % annual cooling energy reduction in tropical climates compared to conventional glass, addressing critical urbanization challenges. This research not only advances the development of adaptive thermochromic windows but also establishes a pioneering material integration paradigm for sustainable architecture, particularly targeting energy-intensive urbanization in tropical regions.

1. Introduction

Smart windows have been extensively studied for their ability to dynamically adjust light transmittance in response to the surrounding environment. These windows can be categorized into several main types based on different external stimuli: temperature-responsive thermochromic [1,2], electrically activated electrochromic [3,4], light-responsive photochromic [5,6], and mechanically induced mechanochromic [7,8]. Among these, thermochromic smart windows, which switch between colored and bleached states with temperature changes, are highly favored due to their passive regulation behavior that requires no additional energy input to trigger thermochromism, as well as their simple configuration and low cost [2]. Organic-inorganic hybrid perovskites have emerged as promising materials for thermochromic smart windows [9], exhibiting thermochromism in the visible (VIS) wavelength range. Zhang et al. demonstrated a typical perovskite-based thermochromic smart window using H-$MAPbI_3$, achieving a high luminous transmittance (T_{lum}) of 85 % and solar modulation ability (ΔT_{sol}) of 25.5 % [10]. Additionally, vanadium dioxide (VO_2) undergoes a metal-to-insulator transition, enabling transmittance modulation in the near-infrared (NIR) region, with a reported transmittance reduction of 41.5 % at 2000 nm above its transition temperature ($\tau_s \sim 68\,^{\circ}C$) [11,12]. Current research on VO_2 focuses on enhancing its ΔT_{sol}. Studies have demonstrated that gradient variation oxygen-content vanadium-oxygen composite films can achieve a modulation rate of 16.8 % [13]. Additionally, the integration of VO_2 with other materials has garnered significant attention. For instance, existing studies have utilized VO_2 combined with paraffin to achieve three-phase independent modulation of solar bands [14], while combining VO_2 with WO_3 enables tri-band full-spectrum independent modulation through electrochromism [15].

* Corresponding authors.
E-mail addresses: johnnyho@cityu.edu.hk (J.C.Y. Ho), chiytso@cityu.edu.hk (C.Y. Tso).

[1] These authors contributed equally to the work.

https://doi.org/10.1016/j.cej.2025.164738
Received 8 April 2025; Received in revised form 27 May 2025; Accepted 10 June 2025
Available online 10 June 2025
1385-8947/

However, existing thermochromic smart windows often operate within specific, fixed solar bands, which significantly limits their overall energy-saving potential and practical applicability [16,17]. Recent advances in thermochromic smart windows leverage VO_2's dual functionality: NIR transmittance modulation and mid-infrared (MIR) emissivity control via Fabry-Pérot resonance. The Fabry-Pérot structure, formed by a dielectric layer inserted between the temperature-adaptive VO_2 layer and a highly reflective bottom layer, creates a multilayer resonator that achieves emissivity modulation [18–20]. For example, a $TiN/Al_2O_3/VO_2$ structure on a Si substrate has demonstrated thermal emissivity control of ~48 % [21], while a VO_2/BaF_2/Gold configuration has shown ~47 % switchability [22]. However, these designs primarily focus on the thermal radiation behavior of structures as emitters, with limited consideration of T_{lum} for window applications. To address this issue, some research efforts were made to replace the bottom-metal reflector with transparent Indium tin oxide (ITO), yielding T_{lum} of 27.8 % and ΔT_{sol} of 9.8 % while maintaining reasonable emissivity modulation [23]. Similarly, a wood-based structure has achieved 44 % emissivity modulation with a T_{lum} of 20.3 % [24]. However, the energy-saving performance of these studies remains limited due to their inability to achieve effective regulation in the VIS light spectrum, which constitutes approximately 43 % of solar radiation energy [25]. Recognizing the limitations of spectrally restricted modulation, the concept of a Full-spectrum Modulated Smart Window (FMSW) has emerged, integrating solar transmittance and atmospheric window emissivity modulation. An ideal FMSW necessitates spectrally selective control over VIS (380–780 nm), NIR (780–2500 nm), and MIR (2.5–25 μm) wavelengths to adaptively regulate solar heat and radiative cooling across variable climatic conditions. During winter operation (cold state), optimal VIS transmittance preserves daylighting and thermal efficiency, while elevated NIR transmittance maximizes solar heat gain. Concurrently, low MIR emissivity minimizes radiative heat loss as indicated by Fig. 1a.

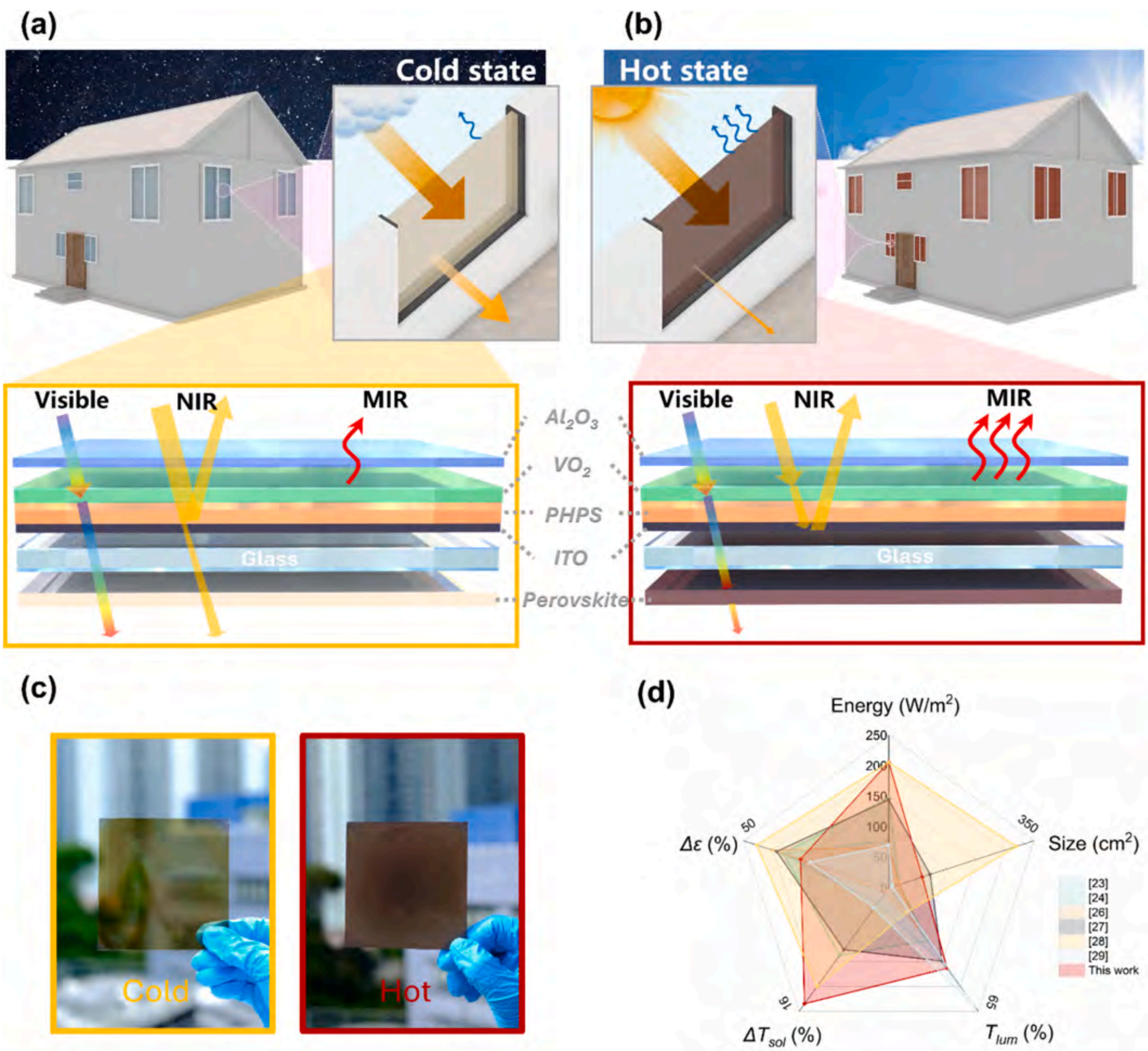

Fig. 1. (a, b) Schematic illustration of the proposed FMPSW integrated into buildings and its functionality from VIS to MIR in the (a) cold and (b) hot states, respectively. (c) Outdoor photographs of the proposed FMPSW with dimensions of 10×10 cm^2 in the cold and hot states. (d) Radar map comparing key properties of previous VO_2-based dual-modulation studies with those of this work [23,24,26–29].

In summer, VIS transmission is partially attenuated to reduce solar heat gain from VIS wavelengths, while near-complete NIR blocking mitigates infrared-induced heating. Enhanced MIR emissivity further enables passive radiative cooling by dissipating heat through the atmospheric transparency window as shown in Fig. 1b. Such harmonized wavelength-specific modulation dynamically balances solar harvesting, radiative cooling, and daylight autonomy, potentially further reducing building energy demands in both heating and cooling seasons. The limitations of conventional thermochromic systems lie in their ability to modulate VIS/NIR or to achieve solely the coordinated regulation of NIR and MIR bands. This multispectral design paradigm, however, possesses the potential for simultaneous regulation across these three bands, effectively overcoming the aforementioned limitations.

In this study, we propose an innovative Full-spectrum Modulated Perovskite-based Smart Window (FMPSW) presented in Fig. 1c that utilizes a Fabry-Pérot cavity to synergistically integrate the thermochromic modulation capabilities of $MAPbI_3$ perovskite and VO_2. Systematic Finite Difference Time Domain (FDTD) analysis provides valuable insights into the thickness-dependent optical properties of multilayer structures, elucidates the fundamental physical mechanisms governing the observed phenomena, and establishes optimal thickness configurations to inform and direct subsequent experimental investigations. Experimental results demonstrate that the FMPSW sample (FMPSW-135) with optimal energy-saving potential achieves an emissivity modulation of 33.4 %, a ΔT_{sol} as high as 16.0 %, and a T_{lum} of 42.3 %. Compared to other VO_2-based dual/tri-band modulation devices reported in the literature, as shown in Fig. 1d and Table S1 in the Supporting Information, this work demonstrates the highest energy-saving behavior and maximum ΔT_{sol}. Additionally, its T_{lum}, $\Delta\varepsilon$, and size maintain relatively superior performance, positioning it as a leading candidate for advanced applications. Among the investigated samples, the FMPSW sample with optimized emissivity modulation capability presents a maximum emissivity modulation of 46 % while retaining a luminous transmittance of 39 %. The application feasibility of the proposed structure is thoroughly elucidated through an EnergyPlus energy consumption simulation, which has been meticulously conducted to assess the energy-saving capabilities of a three-floor building that utilizes FMPSWs, in contrast to conventional glazing solutions such as normal glass and low-E glass. This innovative technology not only provides critical insights into multi-spectral modulation but also offers a practical, scalable solution to advance sustainable architectural practices, paving the way for a new era of energy-efficient building design.

2. Materials and methods

2.1. FDTD simulation settings

The optical performance and electromagnetic characteristics of the proposed device in the wavelength range of 0.25 to 16 μm under varying layer thickness are simulated by FDTD with high efficiency and accuracy. Each Al_2O_3/VO_2/PHPS/ITO layer is set as rectangular and initially stacked together. The refractive indices of the PHPS and ITO of 220 nm measured by the IR-VASE ellipsometer are presented in Figs. S1a and b in the Supporting Information, while the refractive indices of Al_2O_3 and VO_2 in the cold and hot states are obtained from previous report [30,31]. The boundary conditions are set as PML in the x, y, and z directions. The chosen plane-wave light source is placed above the top film, while the reflection monitor is placed above the light source. However, the transmittance and reflectance monitors are designed to be located beneath the bottom layer and above the top layer, respectively. Moreover, the electric monitor is set in the ITO layer. Therefore, optical performance and electromagnetic characteristics can be precisely calculated by the FDTD model.

2.2. Materials and fabrication

CH_3NH_3I (MAI, 99.5 %) was from Xi'an Polymer Light Technology. PbI_2 (99 %), DMF (> 99.5 %), and Ethyl Acetate were obtained from Sigma Aldrich and Alfa Aesar, respectively. The ITO glass substrates with different ITO thicknesses were purchased from Guluo Co., Ltd. The V targets used for the sputtering process were from PrMat. Perhydropolysilazane (PHPS) was supplied by Iota Silicone Oil (Anhui) Co., Ltd. Commercial ITO glass with the size of 30 mm × 30 mm × 1.1 mm was used as the thin film substrate for the entire structure. A plasma cleaner first treated the ITO glass substrate with a certain ITO thickness to enhance surface wettability and facilitate surface activation. After that, 100 μL of PHPS was dispensed onto the treated ITO glass surface and subsequently subjected to a spin-coating process at 1000 rpm/2000 rpm/3000 rpm for 20 s to present different PHPS thicknesses, followed by heating on a hot plate at 100 °C for 1 h. Afterward, a metallic V (99.9 %, PrMat) target was used to grow the monoclinic VO_2 films on the prepared PHPS layer by an rf-plasma-enhanced reactive magnetron sputtering instrument with a base pressure better than 1×10^{-7} Torr. During the deposition, the substrate temperature was maintained at 450 °C, and the sputtering power was 110 W with an argon-oxygen flow ratio of 10:1 at a growth pressure of 3×10^{-3} Torr. The growth thickness and rate were simultaneously monitored by a crystal oscillator (SQC-310, INFICON). The prepared sample was then flipped over for further deposition of the perovskite layer. The fabrication of the perovskite layer was conducted in a glovebox (water content ≤1 ppm, oxygen content ≤1 ppm), right after the synthesis of the outdoor (VO_2) side. Lead iodide (PbI_2) and methylammonium iodide (MAI) were dissolved in a dimethylformamide (DMF) solution with a molar ratio of 4.5:1 to form the $MA_4PbI_6{\cdot}2H_2O$ perovskite precursor. Subsequently, the precursor solution was spin-coated at 2000 rpm for 30 s. Prior to this, plasma treatment was also carried out for the indoor (perovskite) side of the sample for the same purpose. The Ethyl Acetate (EA) was dripped during this spin-coating process at the 10^{th} second after starting to spin to form an enhanced surface morphology, creating enhanced luminous transmittance compared to a normal perovskite smart window surface. The entire sample was then annealed at 100 °C for 30 min to accelerate crystallization and remove residual solvents.

2.3. Characterization

2.3.1. Optical characterization

For the proposed structure, there are several parameters that need to be considered regarding energy-saving performance, such as luminous transmittance, solar modulation, and emissivity modulation. These parameters can be tested and calculated as follows: the transmittance spectrum can be recorded by utilizing a UV–vis-NIR spectrometer (1050+, PerkinElmer Lambda), and used for further calculations of luminous transmittance (T_{lum}) and solar modulation ability (ΔT_{sol}) of the entire structure by the following equations:

$$T_{lum}\frac{\int_{\lambda=380nm}^{780nm} y(\lambda)T(\lambda)d\lambda}{\int_{\lambda=380nm}^{780nm} \tau_{lum}d\lambda} \tag{1}$$

$$T_{sol}\frac{\int_{\lambda=250nm}^{2500nm} AM_{1.5}(\lambda)T(\lambda)d\lambda}{\int_{\lambda=250nm}^{2500nm} AM_{1.5}(\lambda)d\lambda} \tag{2}$$

Where $T(\lambda)$ is the tested transmittance spectrum throughout the solar range, $y(\lambda)$ is CIE (International Commission on Illustration) standard for the photonic luminous efficiency of the human eye and $AM_{1.5}$ is the solar irradiance spectrum for an absolute air mass of 1.5 (standard solar irradiance distribution). The difference in solar transmittance between the cold ($T_{sol,cold}$) and the hot state ($T_{sol,hot}$) can be calculated to achieve the solar modulation ability using the following equation: $\Delta T_{sol} = T_{sol,cold} - T_{sol,hot}$. Besides, the reflectance and transmittance spectrum in the range of 2.5–16 μm can be obtained by the FTIR spectrometer (PIKE Technologies 660–10,740,000); thus, the integral emissivity in the atmospheric window (8–13 μm) range of the entire structure can be calculated by the following equations:

$$B(\lambda,T)=\frac{2\pi hc_1^2}{\lambda^5}\frac{1}{e^{\left(\frac{hc_2}{\lambda KT}\right)}-1} \tag{3}$$

$$\varepsilon=\frac{\int_{\lambda=8\mu m}^{13\mu m}(1-R(\lambda))\cdot B(\lambda,T)d\lambda}{\int_{\lambda=8\mu m}^{13\mu m}B(\lambda,T)d\lambda} \tag{4}$$

Where *R(λ)* stands for the tested reflectance in the calculated wavelength range, c_1 (3.7418×10^8 W·μm^4·m^{-2}) and c_2 (1.4388×10^4 μm·K) are the first and second radiation constants, respectively, *h* is the Plank constant ($6.62607015 \times 10^{-34}$ J·s), *K* is the Boltzmann constant (1.380649×10^{-23} J/K), and *T* here represents the corresponding temperature. The desired integral emissivity modulation in the atmospheric window wavelength region between the cold (ε_{cold}) and the hot state (ε_{hot}) can be calculated by the following equation:

$$\Delta\varepsilon=\varepsilon_{hot}-\varepsilon_{cold} \tag{5}$$

2.3.2. Thermal characterization

The transition temperature of the entire sample is tested separately since the transition temperature of the perovskite and VO_2 is not consistent. Firstly, the transition temperature of the perovskite is defined by the first derivative of the transmittance at the specific wavelength in the visible spectrum (λ = 550 nm) with the variation of temperature, which is indicated by the following equation: $\tau_{trans} = \max|dT_{\lambda=550nm}/dt|$, here, $T_{\lambda=550nm}$ and t denotes the transmittance at 550 nm and the applied temperature. The specific transmittance at 550 nm is measured by a Lens Transmittance meter (SDR8508, SpeeDre) with a temperature interval of 2 °C. Similarly, the transition temperature of the VO_2 layer is also defined by the first derivative of the integral emissivity with the variation of temperature: $\tau_{trans} = \max|d\varepsilon/dT_o|$. Here, T_o denotes the applied temperature as well, and the integral emissivity is also measured by the FTIR mentioned before, with a temperature interval of 10 °C. Infrared (IR) images of the samples are captured by FLIR E75 to further ensure the dynamic emissivity modulation of the samples under temperature variations.

2.3.3. Nanostructure, durability, anti-abrasion characterization

The surface morphologies of the indoor and outdoor sides are captured by Scanning Electron Microscopy (SEM, Zeiss EVO M10). The presented HRTEM, HAADF image, EDS mapping, and SAED pattern of the FMPSW sample are tested by a FEI Titan Themis TEM. The crystalline structure of the entire sample is characterized by XRD (XRD PANalytical). The temperature-based Raman spectrum of the entire structure is tested by WITec RAMAN alpha 300R. A repetitive cycle test of 100 heating and cooling processes is conducted in the lab with a surrounding temperature of 23 °C, relative humidity of 70 %, and a heating temperature of 110 °C. After every 10 cycles, the solar transmittance and the emissivity spectrum under cold and hot conditions are tested and recorded accordingly for comparison.

For the anti-abrasion test for the outdoor side, a 10 cm × 10 cm piece of sandpaper is affixed to a flat table surface, and then the outside (VO_2 side) surface of the FMPSW sample is placed in direct contact with the sandpaper. Adhesive tape is used to secure both ends of the sample, and a 500 g weight is positioned on top to maintain uniform contact pressure. The sample is subjected to a reciprocating motion by pulling the right-side tape to slide it from the left edge of the sandpaper to the right, then pulling the left-side tape to return it to the starting position, constituting one complete cycle. Emissivity measurements under cold and hot conditions are conducted after every 5 cycles, with the cold and hot state emissivity results of each cycle documented accordingly.

3. Results and discussion

3.1. Structural design and operation principle of the proposed FMPSW

The configuration of the proposed FMPSW, as presented in Fig. 2a, consists of two main components deposited on either side of a glass substrate. On the indoor side, a hydrated $MA_4PbI_6\cdot 2H_2O$ perovskite layer is deposited, which exhibits transparency in its cold state. Upon heating above its transition temperature, this layer transforms into red-brownish $MAPbI_3$, effectively blocking visible light transmittance [16]. On the outdoor side, a VO_2-based Fabry-Pérot resonant structure is employed, comprising a bottom ITO reflector, a middle PHPS spacer, and a thermochromic VO_2 top layer. In the VO_2-based Fabry-Pérot resonant structure, the monoclinic phase of VO_2, along with the transparency of PHPS and ITO, allows for partial solar light transmission when the ambient temperature $T < \tau_s$, while the bottom ITO reflects incoming MIR light, resulting in relatively high solar transmittance and low MIR absorption. Conversely, when $T > \tau_s$, the rutile phase of VO_2 blocks NIR light and forms a Fabry-Pérot resonant cavity, leading to low NIR transmittance and high absorption in the MIR range. To enhance the luminous transmittance of the FMPSW for improved application feasibility, an Al_2O_3 antireflection layer is adopted above the VO_2 layer, further increasing the cold-state luminous transmittance [32,33]. Thus, the full-spectrum modulation capability from the VIS to the MIR range can be realized through the functionalization of these two distinct thermochromic materials. During cold days, the designed structure achieves high solar transmittance and low MIR emissivity, promoting heat ingress and reducing heat dissipation by thermal radiation. During hot days, the FMPSW exhibits low solar transmittance and high MIR emissivity, preventing solar heat from entering the room while promoting radiant heat dissipation. Overall, the dynamic regulation of the proposed FMPSW in response to temperature variations satisfies indoor comfort requirements and effectively reduces the energy consumption of the building's air conditioning system.

3.2. Simulation validation and optimization of the FMPSW device

To verify the validity of the proposed design and optimize its optical performance across the solar spectrum and MIR range, FDTD simulations were employed. On the indoor side of the FMPSW, the perovskite layer thickness ($\delta_{perovskite}$) was optimized to 800 nm based on previous research findings, which demonstrated superior visible light modulation capability. On the outdoor side, the thickness of the VO_2 layer (δ_{VO_2}) significantly influences luminous transmittance due to its yellow-brownish color. The thickness of the Al_2O_3 antireflective layer ($\delta_{Al_2O_3}$) also plays a crucial role in reducing surface reflections, thereby enhancing overall luminous transmittance. FDTD simulations revealed that when δ_{VO_2} and $\delta_{Al_2O_3}$ were set to 40 nm and 80 nm, respectively, T_{lum} and ΔT_{sol} reached optimal values (Table S2, Supporting Information), satisfying the minimum requirement of 40 % for window applications in commercial buildings as specified by ASHRAE 90.1, while maintaining good solar modulation. Although variations in the thickness of the ITO layer (δ_{ITO}) or PHPS spacer layer (δ_{PHPS}) have minimal impact on overall luminous transmittance due to their high transparency, they do affect the overall solar modulation ability (ΔT_{sol}) and mid-infrared emissivity modulation ($\Delta\varepsilon$) for the following reasons: The thickness of ITO affects optical performance by altering reflectivity in the NIR and MIR regions due to changes in free carrier density and plasmonic effects, impacting ΔT_{sol} and $\Delta\varepsilon$ of the Fabry-Pérot structure. The thickness of PHPS influences optical performance by tuning the resonant wavelength and controlling the phase shift of reflected waves, enabling optimal absorption and broadband absorbance in the 8–13 μm range.

To thoroughly investigate the effects of δ_{ITO} and δ_{PHPS} variations on optical properties, five ITO thicknesses (ranging from 380 nm to 60 nm) and five PHPS thicknesses (ranging from 1250 nm to 250 nm) were

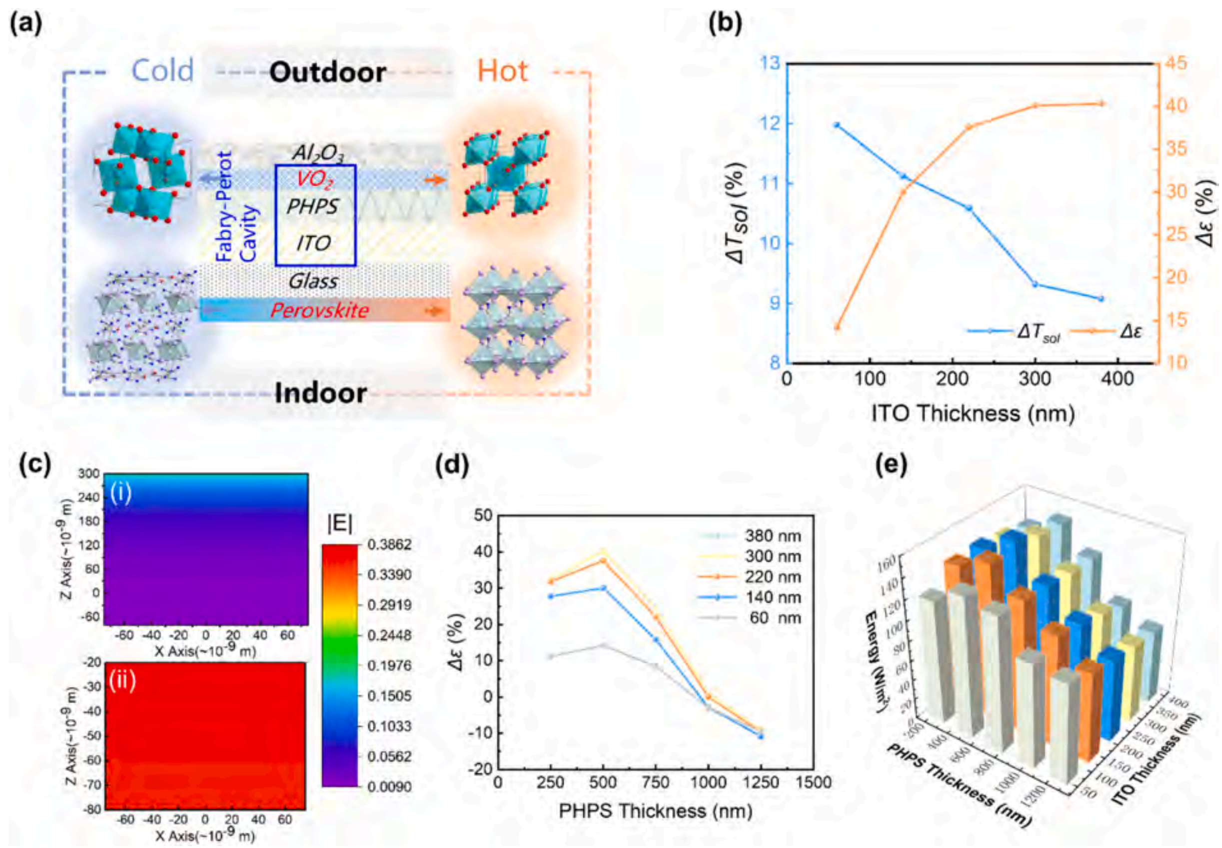

Fig. 2. FDTD Simulation results of the proposed FMPSW. (a) Schematic layout of the FMPSW structure in two states. (b) Variations in ΔT_{sol} and $\Delta\varepsilon$ of samples with fixed δ_{PHPS} at 500 nm and different δ_{ITO} values. (c) Electric field distribution at $\lambda = 8$ μm within the ITO layer for samples with $\delta_{ITO} = 380$ nm (i) and 60 nm (ii), respectively. (d) Variations in $\Delta\varepsilon$ for the 25 simulated samples. (e) Calculated Energy values based on the 25 simulated results with varying δ_{ITO} and δ_{PHPS}.

selected based on previous Fabry-Pérot structure studies [27,28,34], forming 25 thickness combinations. These combinations offer a comprehensive analysis of the interplay between the solar modulation and the emissivity modulation capability of FMPSWs. Firstly, all simulation results presented effective full-spectrum modulation capability of the proposed structure from the VIS to MIR range, confirming the efficacy of this design (Fig. S2, Supporting Information). Additionally, the rules of modulation in optical parameters induced by variations in δ_{ITO} and δ_{PHPS} are rigorously examined. Specifically, when δ_{PHPS} is fixed, an increase in δ_{ITO} reveals a trade-off relationship as ΔT_{sol} diminishes and $\Delta\varepsilon$ concurrently increases, while the luminous transmittance of the overall structure remains unchanged. As illustrated in Fig. 2b, when δ_{ITO} ranges from 60 nm to 380 nm, while maintaining δ_{PHPS} at a constant 500 nm, ΔT_{sol} decreases from 12 % to 9 %. Simultaneously, $\Delta\varepsilon$ shows a substantial increase from 13 % to 40 %, and the overall luminous transmittance remains consistent around 45 % across diverse δ_{ITO}. Changes in optical performance for the overall structure due to δ_{ITO} variations can be explained by the following mechanisms: In the solar spectral range, an increase in δ_{ITO} typically enhances the free carrier density of ITO due to improved crystallinity or reduced defect density during deposition. The strong interactions between free carriers and incident light amplify the plasmonic effect on the ITO surface, thereby increasing the reflection of NIR light from the structure and consequently reducing NIR transmittance. Consequently, the modulation ability of thermochromic VO_2 in the NIR range will become less pronounced, ultimately resulting in a decrease in the ΔT_{sol} of the proposed structure. This interplay suggests that a thicker ITO layer not only exacerbates the attenuation of NIR transmittance of the FMPSW but also significantly narrows its transmittance differential between the hot and cold states. While in the MIR range, the variations in $\Delta\varepsilon$ can be attributed to different surface plasmon polaritons (SPPs) excitation within the ITO layer [35,36]. SPPs are electromagnetic excitations that arise at the interface between a metal and a dielectric material [37]. The resonant interactions between SPPs and electromagnetic radiation at metal-dielectric interfaces will amplify the optical near field [38,39], thus significantly enhancing the absorptivity of metallic materials that support them. To investigate the SPPs excitation in the ITO layer, the simulated electric field intensity (|E|) distributions for structures with ITO thicknesses (δ_{ITO}) of 380 nm and 60 nm are presented in Figs. 2c (i) and (ii), respectively. In the cold state, the structure with $\delta_{ITO} = 380$ nm exhibits a lower emissivity compared to that with $\delta_{ITO} = 60$ nm. This reduction is attributed to increased optical losses due to enhanced reflection of incident light with thicker ITO layers, which suppresses its surface plasmon resonance effect and consequently diminishes SPPs excitation. The reduced SPPs excitation results in a lower electric field intensity at the structure's surface, with |E| values of 1.17 for δ_{ITO}= 380 nm compared to 1.44 for $\delta_{ITO} = 60$ nm, leading to decreased absorption in the cold state. In contrast, in the hot state, the interplay between the ITO layer's plasmonic resonance and the phase-transition properties of VO_2 within the Fabry-Pérot cavity induces strong interference effects. This Fabry-Pérot resonance dominates the optical response in the MIR region, significantly enhancing absorption. Consequently, the hot-state emissivity is markedly higher than that in the cold state. When the δ_{PHPS} is kept constant, the dominant Fabry-Pérot resonance minimizes the differences in SPPs excitation between samples with varying δ_{ITO}. This is evidenced by the small disparity in surface electric field intensities in the hot state (|E| = 0.456 for $\delta_{ITO} = 380$ nm and |E| = 0.522 for δ_{ITO}= 60 nm), indicating negligible differences in hot-state emissivity between the two structures. Therefore, when δ_{PHPS} remains constant and δ_{ITO} increases, the effective modulation performance ($\Delta\varepsilon$), calculated using Eq. (5), increases accordingly. Analysis of 25 simulated datasets from Table S3 in the Supporting Information reveals that, for samples with identical PHPS thicknesses, the hot-state emissivity remains nearly constant across different δ_{ITO} values. However, in the cold state, emissivity decreases progressively with increasing δ_{ITO}.

Besides, when δ_{ITO} is fixed, δ_{PHPS} primarily influences $\Delta\varepsilon$ as well. As demonstrated in Fig. 2d, the optimal $\Delta\varepsilon$ is consistently observed at δ_{PHPS}= 500 nm. The underlying physical mechanisms can be illustrated as follows: In the solar-spectrum range, fluctuations in δ_{PHPS} do not yield significant alterations in T_{lum} and ΔT_{sol} (Table S3, Supporting Information) due to the high solar transparency of PHPS. However, in the MIR band, the δ_{PHPS} significantly influences the overall emissivity of the structure, as it governs the resonance wavelength tunability of the Fabry-Pérot cavity. The thickness of the spacer layer determines the resonant wavelength (λ_{res}) of the Fabry-Pérot cavity, with a thinner δ_{PHPS} corresponding to a shorter resonance wavelength and a thicker δ_{PHPS} leading to a longer resonance wavelength. The optimal δ_{PHPS} can be precisely calculated using the following Eq. [18]: $\delta_{PHPS} = m\,\lambda_{res}/4n_c$. In this context, m denotes an odd integer, λ_{res} indicates the desired wavelength, and n_c signifies the refractive index of the spacer material. This

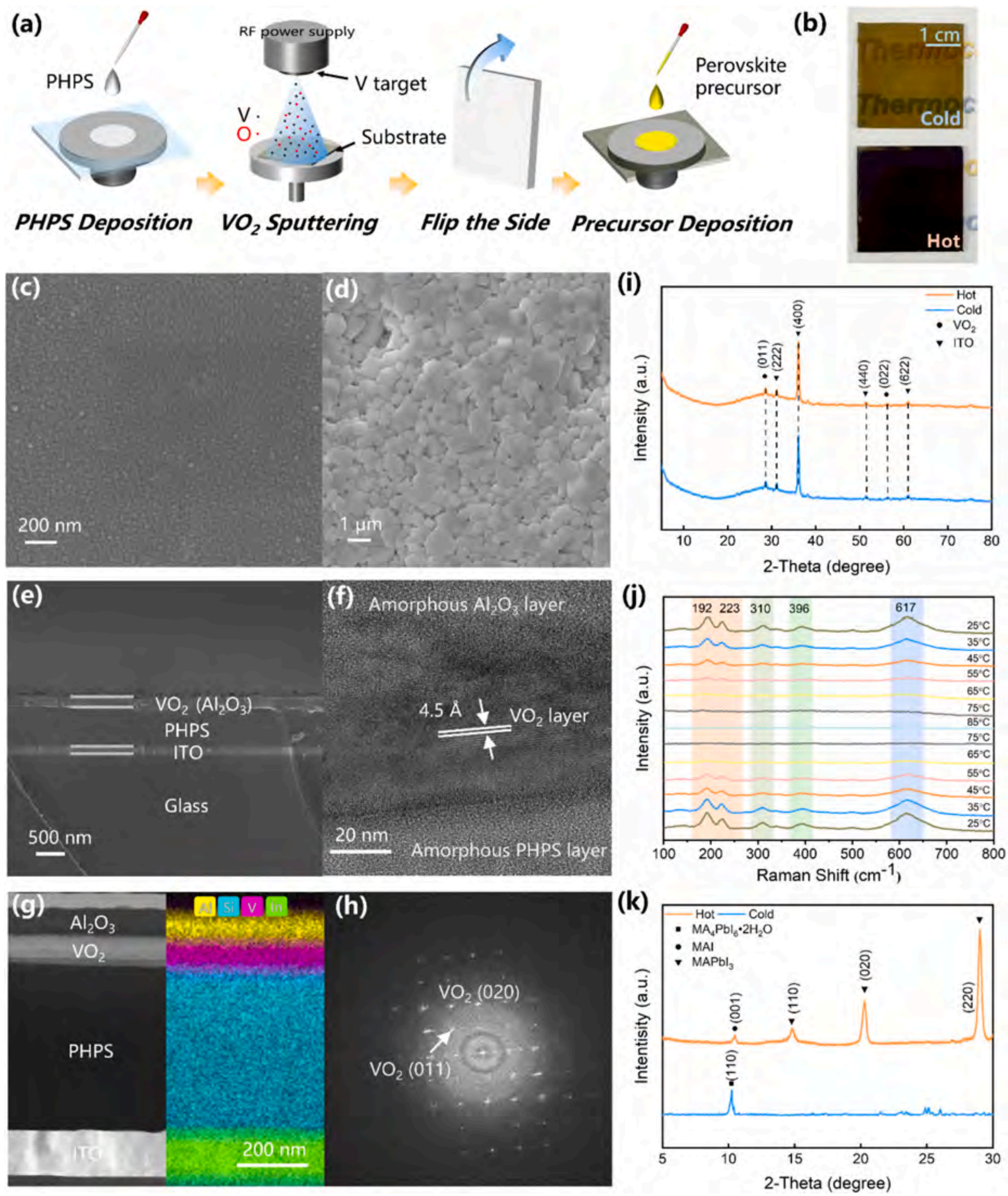

Fig. 3. Material characterization of a fabricated FMPSW sample. (a) Fabrication process. (b) Indoor photographs of a typical FMPSW in the cold and hot states, with dimensions of 3×3 cm^2. (c) SEM surface morphology of the outdoor (VO_2) side. (d) SEM surface morphology of the indoor (perovskite) side. (e) Cross-section SEM image of the outdoor side. (f) High-Resolution TEM of the outdoor side. (g) HAADF analysis and EDS mapping of the outdoor side. (h) SAED pattern analysis of the outdoor side. (i) XRD pattern of the outdoor side. (j) Temperature-dependent Raman spectra of the outdoor side. (k) XRD pattern of the indoor side.

equation indicates that the optimal δ_{PHPS} is determined exclusively by the desired wavelength and the characteristics of the spacer material.

In conclusion, adjusting δ_{ITO} and δ_{PHPS} will enable the entire structure to achieve optimal performance. However, ΔT_{sol} and $\Delta\varepsilon$ are mutually constraining, with each factor impacting energy-saving behaviors to a different extent. Therefore, the synergistic effects of ΔT_{sol} and $\Delta\varepsilon$ in an FMPSW can be initially evaluated using the parameter Energy (E) to quantitatively assess the energy-saving potential. Assuming a standard solar irradiation power of 1000 W/m^2 and a blackbody surface emissive power of 140 W/m^2 through the atmospheric window [40], the energy-saving potential E can be evaluated as $E = 1000 \times \Delta T_{sol} + 140 \times \Delta\varepsilon$. The equation is designed to quantify the net heat load reduction achieved by the material's ability to reduce solar heat input (ΔT_{sol}) and enhance radiative heat dissipation ($\Delta\varepsilon$). It assumes continuous peak power for both solar (1000 W/m^2) and thermal (140 W/m^2) radiation under ideal conditions, such as summer midday in Hong Kong, and blackbody emissions. By summing these positive contributions, the equation represents the theoretical maximum cooling energy savings of the entire structure in its thermally phase-changed state and quantifies its optimal energy-saving potential. Based on this formula, the E values of the aforementioned 25 combinations are depicted in Fig. 2e. The highest Energy value is obtained with δ_{ITO}= 220 nm and δ_{PHPS}= 500 nm. Based on these two thicknesses, corresponding samples will be fabricated accordingly in the experiments to further validate their performance. The simulation results highlight the critical role of thickness optimization in determining the transmittance and emissivity behavior, indicating that this optimization is essential before advancing to the subsequent fabrication process.

3.3. Microstructure and optical performance of the FMPSWs

The optimal energy-saving behavior for the FMPSW can be obtained when δ_{ITO}= 220 nm and δ_{PHPS}= 500 nm, as indicated by the simulation results. Consequently, following the methodology outlined in Fig. 3a (see the detailed procedures in the Materials and Fabrication section), δ_{VO_2} and $\delta_{Al_2O_3}$ can be controlled by the sputtering time and samples with varying δ_{PHPS} were initially fabricated while maintaining a fixed δ_{ITO} of 220 nm realized by a commercial ITO glass (see properties of different commercial ITO glasses in Table S4, Supporting Information). Afterward, samples with different δ_{ITO} were prepared while maintaining δ_{PHPS}= 500 nm (with a spin-coating speed fixed at 2000 rpm as indicated by Fig. S3 in Supporting Information).

One of these samples was selected for further material characterization to verify the consistency of its composition with the design, and corresponding photographs of the prepared sample in the cold and hot states are presented in Fig. 3b. Given that the FMPSW consists of two thermochromic materials deposited on either side of the glass substrate, the following characterization is conducted separately for each side. For the outdoor side, the surface and cross-section SEM images presented in Fig. 3c and e reveal the microstructure and significant delamination among the layers. It is noteworthy that Fig. 3e distinctly reveals the stratification of glass, ITO, and PHPS, demonstrating excellent structural integration and connectivity. However, both the VO_2 and Al_2O_3 layers exhibit thicknesses below 100 nm, rendering the interface between them scarcely discernible in the SEM image. To gain further insights, a high-resolution TEM of the outdoor (VO_2) side was conducted, as depicted in Fig. 3g. This image clearly shows the Al_2O_3 layer positioned above the VO_2 layer. The high-resolution TEM analysis also demonstrates that the Al_2O_3 and PHPS layers are amorphous, while the VO_2 layer exhibits distinct lattice fringes with a measured interplanar d-spacing of ~4.5 Å (Fig. 3f), corresponding to the (100) crystalline planes [41,42], being deposited between two amorphous layers of Al_2O_3 and PHPS. Additionally, the SAED pattern shown in Fig. 3h reveals an amorphous halo, while the electron diffraction pattern displays diffraction spots corresponding to the (011) and (020) planes [43], confirming that the VO_2 is in a single-crystal monoclinic phase. These findings collectively underscore the structural integrity of the VO_2/Al_2O_3 interface and the crystalline quality of the VO_2 layer. The XRD pattern is given in Fig. 3i to prove the composition of each layer on this side. The observed peaks at 31°, 35.5°, 51°, and 60.7° correspond to the reflections from (222), (400), (440), and (622) planes of ITO, indicating a high level of its crystallinity. The characteristic diffraction peaks presented at 28° and 55.7° align with the reflections from the (011) and (022) planes, which is a good match with VO_2. However, the XRD patterns for the outdoor (VO_2) side in both cold and hot states are identical, so these XRD images demonstrate the composition of the outside side layers and their crystallinity in both cold and hot states, but they are insufficient to conclusively prove a temperature-adaptive phase transition within the VO_2 layer. Therefore, the thermochromic behavior of the as-prepared VO_2 is characterized using Raman spectroscopy, as illustrated in Fig. 3j. Not only do the Raman peaks observed at 192, 223, 310, 396, and 617 cm^{-1} confirm the crystal structure of VO_2, but the intensities of these peaks also vary with temperature (from 25 to 85 °C), and they recover upon subsequent heating. This convincingly demonstrates the reversible thermochromic transition of VO_2.

For the indoor side, the surface and cross-section SEM images are given in Fig. 3d and Fig. S4 (Supporting Information), showcasing the perovskite morphology and layer thickness of ~800 nm. The variations in the XRD patterns at cold (25 °C) and hot (85 °C) temperatures, as shown in Fig. 3k, illustrate the perovskite's phase transformation behavior. Specifically, the distinct peak at $2\theta = 11°$ (110) corresponds to the characteristic peak of dihydrated $MA_4PbI_6{\cdot}2H_2O$ in the cold state. While in the hot state, the characteristic peaks of $MAPbI_3$ are observed at 14.3° (110), 20° (020), and 28° (220), and the peak observed at 11° (001) corresponds to MAI crystalline. This indicates that the dihydrated $MA_4PbI_6{\cdot}2H_2O$ transforms into $MAPbI_3$ crystalline upon heating, in accordance with the thermochromic mechanism of the perovskite layer. The above microstructure characterizations can effectively prove that the materials adopted in each layer of the prepared samples align well with the designed structure and can be successfully integrated to achieve the desired phase transition behavior.

To experimentally validate the effectiveness of the synergistic interaction among the layers in modulating the overall optical performance, several FMPSW samples were prepared. As shown in Figs. S5a and b (Supporting Information), under a certain T_{lum}, the prepared FMPSW samples demonstrate significant modulation effects in VIS and NIR transmittance, as well as MIR emissivity. Compared to samples without the Al_2O_3 layer, as depicted in Figs. S5a and b (Supporting Information), the Al_2O_3 layer can effectively enhance T_{lum} and synergistically enhance ΔT_{sol}. Additionally, the solar spectrum of the FMPSW sample without the perovskite layer (FMSW), as shown in Figs. S5c and d (Supporting Information), confirm the critical role of the perovskite layer in modulating visible light. The VO_2-based Fabry-Pérot structure in FMPSW primarily contributes to the modulation of NIR transmittance and MIR emissivity, where its effect is pronounced compared to the conventional Perovskite-based Smart Window (PSW), as illustrated in Figs. S5e and f (Supporting Information). Prepared FMPSW can also validate the reported relationship between the layer thickness and the optical properties, together with duplicating the optimal results presented by the FDTD simulation. The optical results of samples, as presented in Table S5 (Supporting Information), with varying δ_{PHPS} and a fixed δ_{ITO} of 220 nm, indicate that the maximum $\Delta\varepsilon = 41.83$ % occurs when δ_{PHPS}= 500 nm (with a spin-coating speed of 2000 rpm), coinciding with the highest Energy value by calculation. But if δ_{PHPS} exceeds 500 nm (600 nm) or is <500 nm (350 nm), $\Delta\varepsilon$ is only 18.95 % and 40.25 %, respectively. This finding is consistent with the conclusion drawn from the simulation results. The optical results of samples with different δ_{ITO} and δ_{PHPS}= 500 nm, demonstrate a trade-off relationship between ΔT_{sol} and $\Delta\varepsilon$, mirroring the results from the simulation, as shown in Table S6 (Supporting Information). When δ_{ITO} equals to 380 nm, $\Delta\varepsilon$ can achieve a remarkable 46 % as indicated by Fig. 4a and will drop to 19.7 % when δ_{ITO} equals to 65 nm. While ΔT_{sol} increases from 11.48 % to 16.4

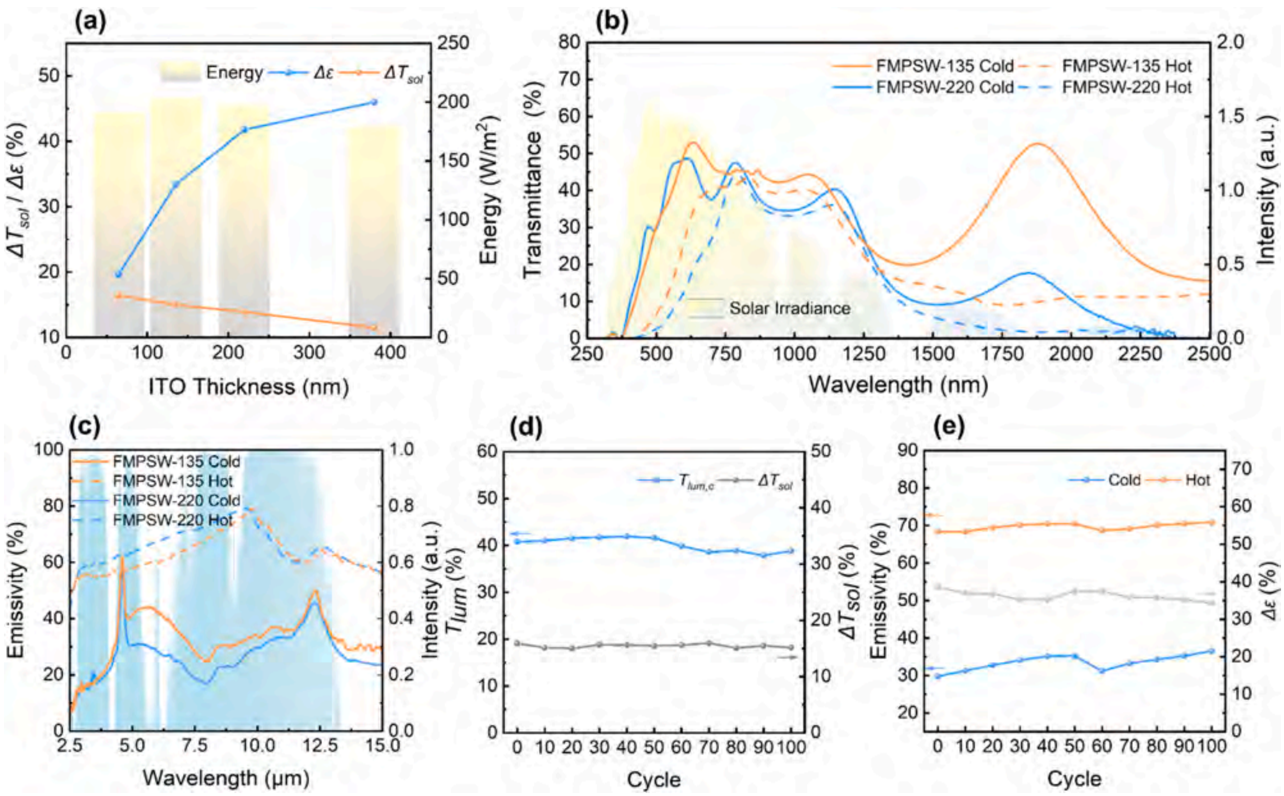

Fig. 4. Optical and thermal properties of FMPSW-135 and FMPSW-220. (a) Variations in ΔT_{sol}, $\Delta\varepsilon$, and Energy values with ITO thicknesses. (b) Transmittance spectra of FMPSW-135 and FMPSW-220 in the solar range in the cold (25 °C) and hot (85 °C) states. (c) Emissivity spectra of FMPSW-135 and FMPSW-220 in the MIR range in the cold (25 °C) and hot (85 °C) states. (d) T_{lum} in the cold (23 °C) and hot (110 °C) states and corresponding ΔT_{sol} performance of FMPSW-135 after cycling. (e) Calculated emissivity values in the cold (23 °C) and hot (110 °C) states and corresponding $\Delta\varepsilon$ performance of FMPSW-135 after cycling.

% when δ_{ITO} changes from 380 nm to 65 nm. However, it was observed that the Energy value for the sample with δ_{ITO}= 135 nm (FMPSW-135) exceeds that of the sample with δ_{ITO}= 220 nm (FMPSW-220), which contradicts the simulation results. To further investigate the optical discrepancies between these two samples, their transmittance (0.25–2.5 μm) and emissivity (2.5–16 μm) spectra are shown in Fig. 4b and c. The obvious transmittance and emissivity contrast between cold and hot states for each sample in the full-spectrum range are observed, which proves the validity of the energy-saving potential of these fabricated samples. Calculated by equations listed in the Characterization section, T_{lum} for FMPSW-135 is 42.30 %, which is similar to 43.07 % of FMPSW-220. FMPSW-135 demonstrates greater modulation in the NIR band compared to FMPSW-220 due to the reduced NIR light reflection from the thinner ITO layer. Therefore, ΔT_{sol} of FMPSW-135 is 15.95 %, while for FMPSW-220 is 13.86 %. Moreover, FMPSW-220 demonstrates a greater emissivity tuning effect compared to FMPSW-135, with $\Delta\varepsilon$ = 41.83 % for FMPSW-220 and $\Delta\varepsilon$ = 33.44 % for FMPSW-135. It was calculated that the Energy value for FMPSW-135 was larger than that of FMPSW-220. When comparing the experimental and simulated data for both samples, the transmittance and emissivity spectra in the solar and MIR bands for FMPSW-220 generally align well with the simulated spectral data, as shown in Figs. S6a and b (Supporting Information). However, there is a significant discrepancy in the experimental and simulated transmittance spectra in the NIR bands for FMPSW-135 as shown in Figs. S6c and d (Supporting Information). This indicates potential variations in the material properties or structural characteristics that may not have been fully captured in the simulations, because the parameter δ_{ITO} plays a crucial role in determining the corresponding refractive index [44]. In our FDTD simulations, the refractive index for the ITO layer was based on an ITO glass with δ_{ITO}= 220 nm. Consequently, inaccuracies may arise when simulating ITO layers of different thicknesses. The dominant contribution of ΔT_{sol} to energy efficiency over $\Delta\varepsilon$ leads to the superior energy-saving performance of FMPSW-135, as the decreased ΔT_{sol} of FMPSW-220 cannot be adequately offset by its substantial improvement in emissivity modulation. Therefore, FMPSW-135 will be further utilized for other property evaluations in the following context.

3.4. Thermal, stability, and mechanical performance of the FMPSW device

To fully understand the performance of thermochromic smart windows, it is critical to examine not only the optical properties in the cold state (25 °C) and hot state (85 °C) but also their variation with ambient temperature. In the proposed FMPSW design, two types of thermochromic materials are incorporated, each with a distinct transition temperature. Previous studies have reported a transition temperature of 68 °C for VO_2 (τ_{sv}) and 45 °C for $MAPbI_3$ (τ_{sp}) [45]. Consequently, the distinct transition temperatures of perovskite and VO_2 divide the optical performance of the overall structure into three temperature-dependent stages. First, when the temperature is below τ_{sp}, the structure remains in a "cold state", exhibiting no thermochromic effects. Second, when the temperature lies between the τ_{sp} and τ_{sv}, only the perovskite layer undergoes a phase transition. In this "warm state", the FMPSW retains its ability to modulate visible light within the VIS spectrum, while the emissivity in the MIR range gradually increases with rising temperature, facilitating moderate heat dissipation. Finally, when the temperature exceeds τ_{sv}, the structure enters a "hot state", where both thermochromic materials undergo phase transitions, resulting in optimal heat shielding and dissipation performance. The τ_s of each thermochromic material in the FMPSW-135 sample were evaluated and calculated using the methods elucidated in the Characterization section. It is evident from Figs. S7 and S8 (Supporting Information) that τ_{sp} is confirmed to be 45 °C, while that for τ_{sv} is 65 °C as presented. Collectively, the three stages defined by these two transition temperatures effectively highlight the device's exceptional temperature-adaptive energy-saving capabilities. To further assess the thermal transition property of the FMPSW-135 sample, its emissivity behavior was evaluated using an infrared (IR) camera. A roughly polished copper plate with a black copper oxide surface, exhibiting an emissivity of approximately 40 %, was used as a reference. At room temperature (25 °C), the emissivity of the FMPSW-135 sample is lower than that of the reference, while at elevated temperatures (100 °C), it surpasses this value. As shown in Fig. S9 (Supporting Information), at room temperature (25 °C), the FMPSW-135 sample displays a lower temperature (24.3 °C) under the IR camera compared to the reference copper plate (26.1 °C). Conversely, at high temperatures (100 °C), the FMPSW-135 sample exhibits a higher temperature (96.5 °C) than the reference (76.5 °C). These IR imaging results provide further evidence of the dynamic emissivity modulation of the FMPSW-135 sample in response to temperature changes, confirming its ability to transition from low to high emissivity across cold and hot conditions.

In addition to examining the optical and thermodynamic properties of the FMPSW device, the stability and durability should also be assessed. When exposed to an ambient environment, the contamination of humidity and oxygen will affect the durability and stability of the proposed FMPSW since the perovskite layer will darken at high humidity, reducing T_{lum} and losing its phase transition function, while VO_2 will be oxidized to V_2O_5 by oxygen in environmental conditions [46,47], leading to the loss of thermochromism. Cycle tests are thus performed to ensure the applicability of FMPSW in real buildings, making the retention of optical and thermochromic properties across multiple cycles a critical indicator of stability and durability. To evaluate the durability and stability of FMPSW samples under high-temperature and high-humidity conditions following repeated thermal cycling, the FMPSW-135 sample was subjected to heating and cooling cycles at an ambient temperature of 23 °C and a relative humidity of 70 %. T_{lum}, ΔT_{sol}, ε, and $\Delta\varepsilon$ of the FMPSW-135 sample were recorded in both hot (110 °C) and cold states (23 °C). As shown in Fig. 4d, the values of $T_{lum,c}$ (cold state luminous transmittance) and ΔT_{sol} remained stable after 100 cycles, effectively demonstrating the stability and durability of the perovskite layer under harsh conditions. Since the $\Delta\varepsilon$ is directly linked to the thermochromic performance of the VO_2 layer, monitoring emissivity fluctuations over multiple cycles confirms its stability and durability. Fig. 4e illustrates that the emissivity values of FMPSW-135 are consistently maintained around 71 % in the hot state and 38 % in the cold state after 100 cycles, further highlighting the stability and durability of the outdoor (VO_2) side. In conclusion, the cycle test results clearly show that the entire FMPSW-135 sample can withstand substantial heating and cooling cycles while consistently delivering stable and effective thermochromic performance.

Given that the outer surface of the FMPSW device comprises a multilayer structure ($Al_2O_3 + VO_2 +$ PHPS+ITO + Glass), it is critical to evaluate the potential for delamination under external forces, such as friction, which could impair the sample's functional performance. To address this, an anti-abrasion test was conducted by the abrasive interaction between the sample's multilayer surface and sandpaper under the pressure of a weight, as depicted in Figs. S10a and b (Supporting Information). The experimental details are provided in the Characterization section. Emissivity measurements of the FMPSW-135 sample in both cold and hot states were recorded over 50 abrasion cycles. The value of emissivity modulation, measured at intervals of every five cycles, served as an indicator to evaluate the sample's functional integrity and detect potential delamination. As shown in Fig. S10c (Supporting Information), the emissivity modulation ability remained stable at approximately 32–33 % across all 50 cycles, with no discernible decline, indicating robust mechanical properties against abrasion and demonstrating the FMPSW sample's suitability for practical applications.

3.5. EnergyPlus simulation of the demonstrative FMPSW-135

To evaluate the energy savings of the proposed FMPSW in actual buildings compared to normal and low-E glass, EnergyPlus simulation was employed to give specific energy consumption of a three-story office building (shown in Fig. 5a) with a total floor area of 4982 m^2, as designed by the U.S. Department of Energy (DOE). The building parameters are summarized in Table S7 (Supporting Information). Three core cities of Beijing, Shanghai, and Hong Kong were selected for simulation because Beijing is located in a cold climate, necessitating greater heating demand, while Shanghai, positioned as a central city, experiences both heating and cooling demands throughout the year. Hong Kong, as a sub-tropical city, has a higher cooling demand, as shown in Fig. 5b the latitudinal differences. Furthermore, the optical properties of normal glass, low-E glass, and FMPSW are shown in Table S8 (Supporting Information). It is worth noting that the transition temperature of the FMPSW in this simulation is established at 45 °C rather than the measured 65 °C. This adjustment is necessary because the FMPSW cannot fully exploit its full-spectrum modulation function, even under the highest simulated city temperatures. Instead, it only drives the phase transition of the perovskite, significantly limiting its practical applicability. To accurately simulate the energy-saving benefits of full-spectrum modulation, the FMPSW's transition temperature is set at 45 °C, below which neither material changes color, while both materials undergo a simultaneous phase transition above this threshold. Experimental studies indicate that the transition temperature of VO_2 can be effectively reduced to around 45 °C through doping VO_2 with 1 % wt. tungsten [48–50], aligning it with the perovskite's transition temperature. Furthermore, increasing the tungsten doping level to 2 wt% can reduce the VO_2 transition temperature to 36.5 °C, which is further below that of perovskite, enabling multi-stage regulation [51]. This advancement can facilitate future research on dynamic full-spectrum modulation. Consequently, the decision here to set the transition temperature at 45 °C in the EnergyPlus simulation is warranted.

The simulation results in Fig. 5c illustrate the cooling, heating, lighting, and total energy consumption of the simulated building in Beijing, Shanghai, and Hong Kong using normal glass, low-E glass, and the FMPSW-135. In all three cities, the energy consumption associated with low-E glass and FMPSW-135 is lower than that of normal glass during the summer for cooling. As presented in Fig. 5d, in Beijing, the use of low-E glass and FMPSW-135 results in cooling load savings of 11.13 % and 28.15 % compared to normal glass, respectively. In Shanghai, these savings are 9.40 % and 24.50 %, while in Hong Kong, they are 8.90 % and 22.66 %, respectively. The results also indicate that FMPSW exhibits higher energy efficiency compared to low-E glass due to its blockage of solar light and high emission in the atmospheric window in the hot state, as shown by its optical properties stated in the previous text. However, in cities that require winter heating, such as Beijing and Shanghai, the energy consumption for heating with FMPSW is slightly higher than that of normal and low-E glass. This is attributed to the inherent coloration of FMPSW, which can prevent the entry of solar radiation that can warm the room in winter. Nevertheless, the low emissivity characteristic of FMPSW windows mitigates heat loss, partially compensating for this increased energy demand. Ultimately, an analysis of total annual energy consumption reveals that the savings in cooling energy effectively counterbalance the rise in heating energy consumption, resulting in a net reduction in overall energy use compared to both normal and low-E glass. Meanwhile, for sub-tropical climates like Hong Kong, where buildings are predominantly cooled throughout the year, and cooling energy constitutes over 30 % of total building energy consumption, FMPSW presents a promising solution for reducing cooling energy usage. As demonstrated in Fig. 5e, the monthly cooling energy consumption with FMPSW-135 is lower than that of both normal glass and low-E glass, providing strong evidence that the energy efficiency of buildings is enhanced by this technology. The simulation results indicate that the implementation of the proposed FMPSW in

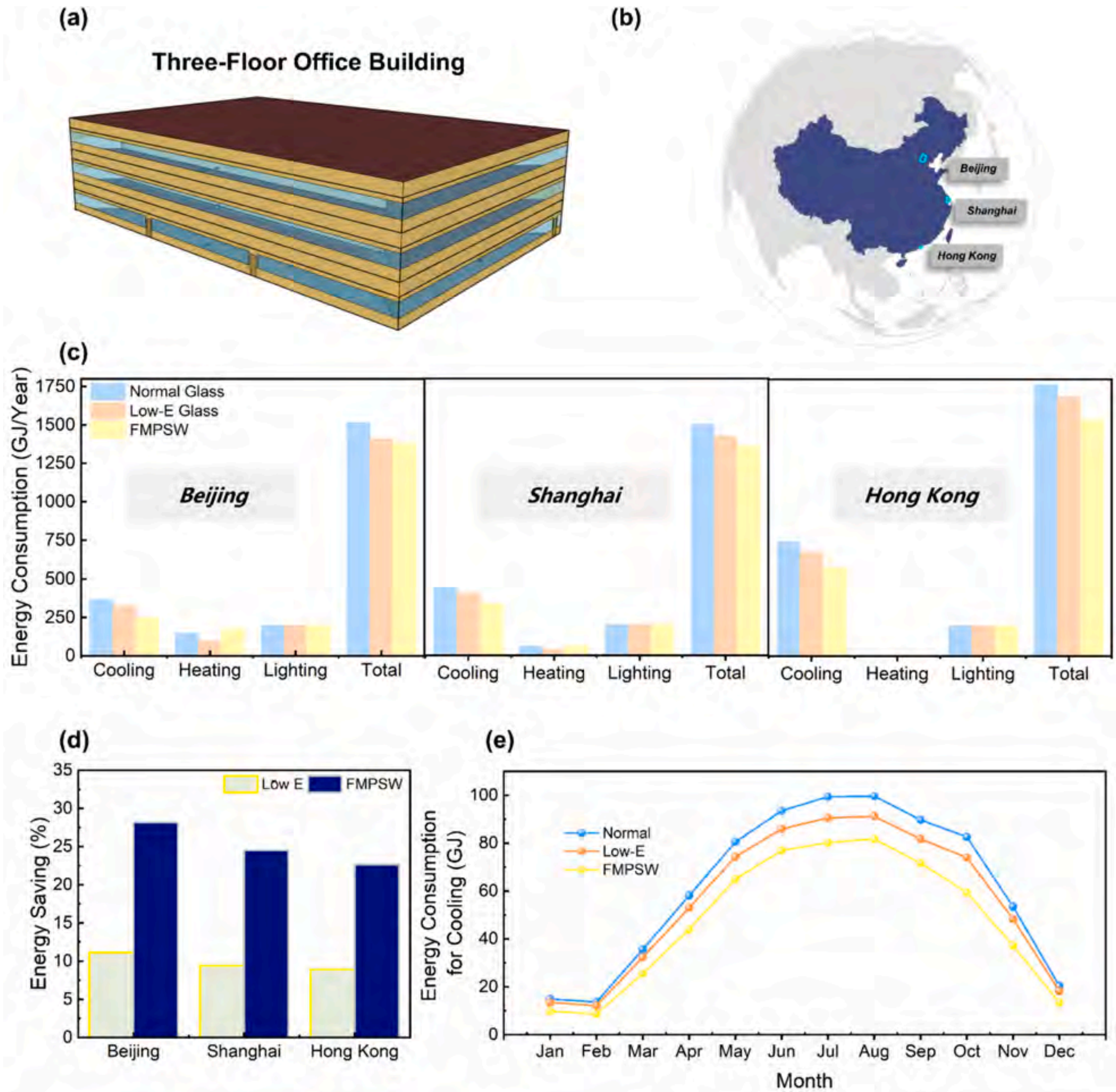

Fig. 5. Simulated energy-saving behavior in a three-floor building. (a) Three-floor building model utilized in EnergyPlus simulation. (b) Geographic locations of Beijing, Shanghai, and Hong Kong. (c) Specific energy consumption for Cooling, Heating, Lighting, and Total in the building. (d) Cooling energy savings from using low-E windows and FMPSW-135 compared to normal windows. (e) Monthly cooling energy consumption values for normal windows, low-E windows, and FMPSW-135 in Hong Kong.

cities across diverse climatic conditions can significantly reduce building energy consumption and will substantially lower carbon emissions.

4. Conclusion

This study presents a novel Full-spectrum Modulated Perovskite-based Smart Window (FMPSW) capable of dynamically regulating optical properties across the VIS to MIR spectrum through the strategic integration of dual thermochromic materials. The proposed system exhibits temperature-responsive performance, achieving optimal thermal management by maintaining high luminous transmittance with low emissivity in winter conditions while transitioning to low luminous transmittance during summer periods with high emissivity behavior. Through systematic FDTD simulations, we identified the optimal interlayer thickness configuration, and the fabricated FMPSW-135 prototype achieved superior energy-saving performance with T_{lum}= 42.30 %, ΔT_{sol}= 16 %, and $\Delta\varepsilon$ = 33.4 %. Experimental results further revealed a maximum $\Delta\varepsilon$ of 46 % with an optimized ITO layer thickness of 380 nm. EnergyPlus simulations confirmed the practical energy-saving potential of the FMPSW in real building applications, demonstrating a significant 22.66 % reduction in cooling energy consumption compared to conventional glass across various weather conditions in Hong Kong. This research provides a solid foundation for the development of full-spectrum adjustable and composite thermochromic-transformative smart windows in the future, offering valuable theoretical and practical insights for advancing energy-efficient building technologies and contributing to global efforts in energy conservation and greenhouse gas emission reduction.

CRediT authorship contribution statement

Qiuyi Shi: Writing – original draft, Validation, Software, Methodology, Investigation, Formal analysis, Data curation, Conceptualization. **Bowen Li:** Writing – review & editing, Visualization, Validation, Resources. **Yuwei Du:** Writing – review & editing, Validation, Formal analysis, Conceptualization. **Sai Liu:** Methodology, Conceptualization. **Rui Zhang:** Investigation. **Cancheng Jiang:** Writing – review & editing, Visualization. **Xin Li:** Writing – review & editing, Data curation. **Muhammad Fahim:** Writing – review & editing. **Irum Firdous:** Writing – review & editing. **Johnny C.Y. Ho:** Writing – review & editing, Funding acquisition. **Chi Yan Tso:** Writing – review & editing, Supervision, Funding acquisition.

Declaration of competing interest

The authors declare that they have no known competing financial interests or personal relationships that could have appeared to influence the work reported in this paper.

Acknowledgments

Q.S. and B.L. contributed equally to this work. C.Y.T. acknowledges financial support from the Hong Kong Research Grant Council (RGC) via the General Research Fund (GRF) account of 11200121 and the RGC Research Fellow Scheme (RFS) via project number RFS2425-1S06. This work was also financially supported by the City University of Hong Kong (Project no. 7020088), the Basic Research Project of the Science and Technology Innovation Commission of Shenzhen (No. JCYJ20230807114910021), and was jointly supported by the Shenzhen Research Institute, City University of Hong Kong.

Appendix A. Supplementary data

Supplementary data to this article can be found online at https://doi.org/10.1016/j.cej.2025.164738.

Data availability

Data will be made available on request.

References

[1] M. Kamalisarvestani, R. Saidur, S. Mekhilef, F.S. Javadi, Performance, materials and coating technologies of thermochromic thin films on smart windows, Renew. Sust. Energ. Rev. 26 (2013) 353–364, https://doi.org/10.1016/j.rser.2013.05.038.

[2] Z. Zhang, L. Zhang, Y. Zhou, Y. Cui, Z. Chen, Y. Liu, J. Li, Y. Long, Y. Gao, Thermochromic energy efficient windows: fundamentals, recent advances, and perspectives, Chem. Rev. 123 (2023) 7025–7080, https://doi.org/10.1021/acs.chemrev.2c00762.

[3] S. Wu, H. Sun, M. Duan, H. Mao, Y. Wu, H. Zhao, B. Lin, Applications of thermochromic and electrochromic smart windows: materials to buildings, Cell Rep. Phys. Sci. 4 (2023) 101370, https://doi.org/10.1016/j.xcrp.2023.101370.

[4] R. Huang, Y. Xie, N. Cao, X. Jia, D. Chao, Self-powered electrochromic smart window helps net-zero energy buildings, Nano Energy 129 (2024) 109989, https://doi.org/10.1016/j.nanoen.2024.109989.

[5] W. Meng, J. Wang, L. Jiang, Recent advances in photochromic smart windows based on inorganic materials, Responsive Mater. 2 (2024) e20240001, https://doi.org/10.1002/rpm.20240001.

[6] T. Ma, B. Li, S. Tian, J. Qian, L. Zhou, Q. Liu, B. Liu, X. Zhao, G. Sankar, Reversible photochromic $W_{18}O_{49}$: mechanism revealing and performance improvement for smart windows, Chem. Eng. J. 468 (2023) 143587, https://doi.org/10.1016/j.cej.2023.143587.

[7] B. Chen, Q. Feng, W. Liu, Y. Liu, L. Yang, D. Ge, Review on Mechanoresponsive smart windows: structures and driving modes, Materials 16 (2023) 779, https://doi.org/10.3390/ma16020779.

[8] F. Zhao, M. Wang, Z. Huang, M. Zhu, C. Chen, Q. Pan, B. Yu, Y. Wang, X. Guo, Y. Qian, L. Zhang, X. Qiu, S. Sheng, Z. He, J. Wang, S. Yu, Bio-inspired mechanically responsive smart windows for visible and near-infrared multiwavelength spectral modulation, Adv. Mater. (2024) 2408192, https://doi.org/10.1002/adma.202408192.

[9] H. He, S. Liu, Y. Du, R. Zhang, T.C. Ho, C.Y. Tso, Enhancing stability: two-dimensional Thermochromic perovskite for smart windows in building applications, Adv. Funct. Mater. (2024) 2417582, https://doi.org/10.1002/adfm.202417582.

[10] Y. Zhang, C.Y. Tso, J.S. Iñigo, S. Liu, H. Miyazaki, C.Y.H. Chao, K.M. Yu, Perovskite thermochromic smart window: advanced optical properties and low transition temperature, Appl. Energy 254 (2019) 113690, https://doi.org/10.1016/j.apenergy.2019.113690.

[11] L. Kang, Y. Gao, H. Luo, A novel solution process for the synthesis of VO_2 thin films with excellent Thermochromic properties, ACS Appl. Mater. Interfaces 1 (2009) 2211–2218, https://doi.org/10.1021/am900375k.

[12] X. Ao, B. Li, B. Zhao, M. Hu, H. Ren, H. Yang, J. Liu, J. Cao, J. Feng, Y. Yang, Z. Qi, L. Li, C. Zou, G. Pei, Self-adaptive integration of photothermal and radiative cooling for continuous energy harvesting from the sun and outer space, Proc. Natl. Acad. Sci. USA 119 (2022) e2120557119, https://doi.org/10.1073/pnas.2120557119.

[13] Z. Li, C. Cao, M. Li, L. Wang, D. Zhu, F. Xu, A. Huang, P. Jin, L. Yu, X. Cao, Gradient variation oxygen-content vanadium–oxygen composite films with enhanced crystallinity and excellent durability for smart windows, ACS Appl. Mater. Interfaces 15 (2023) 9401–9411, https://doi.org/10.1021/acsami.2c21188.

[14] Y. Jiao, Z. Li, C. Li, C. Cao, A. Huang, P. He, X. Cao, Flexible tri-state-regulated thermochromic smart window based on $W_xV_{1-x}O_2$/paraffin/PVA composite film, Chem. Eng. J. 497 (2024) 154578, https://doi.org/10.1016/j.cej.2024.154578.

[15] Z. Shao, A. Huang, C. Cao, X. Ji, W. Hu, H. Luo, J. Bell, P. Jin, R. Yang, X. Cao, Tri-band electrochromic smart window for energy savings in buildings, Nat. Sustain. 7 (2024) 796–803, https://doi.org/10.1038/s41893-024-01349-z.

[16] S. Liu, Y. Du, R. Zhang, H. He, A. Pan, T.C. Ho, Y. Zhu, Y. Li, H. Yip, A.K.Y. Jen, C. Y. Tso, Perovskite smart windows: the light manipulator in energy-efficient buildings, Adv. Mater. (2023) 2306423, https://doi.org/10.1002/adma.202306423.

[17] C. Jiang, L. He, Q. Xuan, Y. Liao, J.-G. Dai, D. Lei, Phase-change VO_2-based thermochromic smart windows, Light Sci. Appl. 13 (2024) 255, https://doi.org/10.1038/s41377-024-01560-9.

[18] S. Taylor, Y. Yang, L. Wang, Vanadium dioxide based Fabry-Perot emitter for dynamic radiative cooling applications, J. Quant. Spectrosc. Radiat. Transf. 197 (2017) 76–83, https://doi.org/10.1016/j.jqsrt.2017.01.014.

[19] S. Liang, F. Xu, W. Li, W. Yang, S. Cheng, H. Yang, J. Chen, Z. Yi, P. Jiang, Tunable smart mid infrared thermal control emitter based on phase change material VO_2 thin film, Appl. Therm. Eng. 232 (2023) 121074, https://doi.org/10.1016/j.applthermaleng.2023.121074.

[20] S. Chen, Z. Wang, H. Ren, Y. Chen, W. Yan, C. Wang, B. Li, J. Jiang, C. Zou, Gate-controlled VO_2 phase transition for high-performance smart windows, Sci. Adv. 5 (2019) eaav6815, https://doi.org/10.1126/sciadv.aav6815.

[21] H. Kim, D. Lahneman, C. Rohde, A. Piqué, VO_2-based thin-film radiators with variable thermal emissivity, Thin Solid Films 759 (2022) 139455, https://doi.org/10.1016/j.tsf.2022.139455.

[22] H. Kim, K. Cheung, R.C.Y. Auyeung, D.E. Wilson, K.M. Charipar, A. Piqué, N. A. Charipar, VO_2-based switchable radiator for spacecraft thermal control, Sci. Rep. 9 (2019) 11329, https://doi.org/10.1038/s41598-019-47572-z.

[23] S. Wang, T. Jiang, Y. Meng, R. Yang, G. Tan, Y. Long, Scalable thermochromic smart windows with passive radiative cooling regulation, Science 374 (2021) 1501–1504, https://doi.org/10.1126/science.abg0291.

[24] X. Hu, W. Cai, Y. Zhang, S. Shi, Y. Ming, R. Yu, D. Chen, M. Yang, F. Wang, H. Yang, C.-W. Kan, N. Noor, B. Fei, Facile and widely applicable route to self-adaptive emissivity modulation: energy-saving demonstration with transparent wood, Nano Lett. 24 (2024) 657–666, https://doi.org/10.1021/acs.nanolett.3c03711.

[25] D. Brune (Ed.), Radiation: at home, outdoors and in the workplace, Scandinavian Science, Oslo, 2001.

[26] S. Bhupathi, S. Wang, G. Wang, Y. Long, Porous vanadium dioxide thin film-based Fabry−Perot cavity system for radiative cooling regulating thermochromic windows: experimental and simulation studies, Nanophotonics (2024), https://doi.org/10.1515/nanoph-2023-0716.

[27] J. Keum, J. Choi, S. Kim, G. Kang, B. Lee, M.J. Lee, W. Kim, Innovative dual-band energy-efficient smart windows using VO_2(M)-based Fabry-Pérot structures for solar and radiative cooling modulation, Mater. Today Phys. (2025) 101665, https://doi.org/10.1016/j.mtphys.2025.101665.

[28] J. Li, C. Zhang, Y. Chen, K. Jiao, Z. Chen, Y. Liu, Y. Gao, Z. Zhang, Fabry–Pérot cavity smart windows with superior solar and thermal modulation capabilities, J. Mater. 11 (2025) 100871, https://doi.org/10.1016/j.jmat.2024.03.015.

[29] C. Li, C. Cao, Z. Li, X. Ji, P. Jin, X. Cao, Dual-functional tunable emitter with high visual transparency for energy saving and information encryption, Appl. Mater. Today 39 (2024) 102297, https://doi.org/10.1016/j.apmt.2024.102297.

[30] J. Houska, J. Blazek, J. Rezek, S. Proksova, Overview of optical properties of Al_2O_3 films prepared by various techniques, Thin Solid Films 520 (2012) 5405–5408, https://doi.org/10.1016/j.tsf.2012.03.113.

[31] R. Beaini, B. Baloukas, S. Loquai, J.E. Klemberg-Sapieha, L. Martinu, Thermochromic VO_2-based smart radiator devices with ultralow refractive index cavities for increased performance, Sol. Energy Mater. Sol. Cells 205 (2020) 110260, https://doi.org/10.1016/j.solmat.2019.110260.

[32] W. Wu, C. Wang, C. Chen, J. Song, F. Ma, Design of Antireflection and Enhanced Thermochromic Properties of TiO_2 /VO_2 thin films, Adv. Mater. Inter. 10 (2023) 2202506, https://doi.org/10.1002/admi.202202506.

[33] S. Liu, C.Y. Tso, H.H. Lee, Y. Zhang, K.M. Yu, C.Y.H. Chao, Bio-inspired TiO_2 nano-cone antireflection layer for the optical performance improvement of VO_2 thermochromic smart windows, Sci. Rep. 10 (2020) 11376, https://doi.org/10.1038/s41598-020-68411-6.

[34] Y. Ou, H. Ji, Y. Wang, B. Liu, Y. Chen, J. Tao, Y. Huang, J. Wang, Photothermal synergistic modulation of patterned VO_2-based composite films for smart windows, Sol. Energy 279 (2024) 112808, https://doi.org/10.1016/j.solener.2024.112808.
[35] P.R. West, S. Ishii, G.V. Naik, N.K. Emani, V.M. Shalaev, A. Boltasseva, Searching for better plasmonic materials, Laser & Photonics Reviews 4 (2010) 795–808, https://doi.org/10.1002/lpor.200900055.
[36] C. Rhodes, M. Cerruti, A. Efremenko, M. Losego, D.E. Aspnes, J.-P. Maria, S. Franzen, Dependence of plasmon polaritons on the thickness of indium tin oxide thin films, J. Appl. Phys. 103 (2008) 093108, https://doi.org/10.1063/1.2908862.
[37] A.V. Zayats, I.I. Smolyaninov, A.A. Maradudin, Nano-optics of surface plasmon polaritons, Phys. Rep. 408 (2005) 131–314, https://doi.org/10.1016/j.physrep.2004.11.001.
[38] S. Wedge, W.L. Barnes, Surface plasmon-polariton mediated light emission through thin metal films, Opt. Express 12 (2004) 3673, https://doi.org/10.1364/OPEX.12.003673.
[39] P. Berini, I. De Leon, Surface plasmon–polariton amplifiers and lasers, Nat. Photon 6 (2012) 16–24, https://doi.org/10.1038/nphoton.2011.285.
[40] A. Felicelli, I. Katsamba, F. Barrios, Y. Zhang, Z. Guo, J. Peoples, G. Chiu, X. Ruan, Thin layer lightweight and ultrawhite hexagonal boron nitride nanoporous paints for daytime radiative cooling, Cell Rep. Phys. Sci. 3 (2022) 101058, https://doi.org/10.1016/j.xcrp.2022.101058.
[41] G. Sun, X. Cao, X. Gao, S. Long, M. Liang, P. Jin, Structure and enhanced thermochromic performance of low-temperature fabricated VO_2/V_2O_3 thin film, Appl. Phys. Lett. 109 (2016) 143903, https://doi.org/10.1063/1.4964432.
[42] X. Li, X. Wang, M. Li, W. Zhu, H. Luo, X. Lu, H. Xu, J. Xue, F. Ye, H. Wu, X. Fan, Built-in electric field enhancement strategy induced by cross-dimensional nano-heterointerface design for electromagnetic wave absorption, Adv. Funct. Mater. (2024), https://doi.org/10.1002/adfm.202407217, 2407217. 2407217.
[43] H. Guo, L. Si, J. Yu, X. Wang, Y. Si, Phase-engineered VO_2 meta nanofiber enables a metal–insulator transition for bidirectional thermal reallocation, Nano Lett. 23 (2023) 6233–6240, https://doi.org/10.1021/acs.nanolett.3c02094.
[44] J.W. Cleary, E.M. Smith, K.D. Leedy, G. Grzybowski, J. Guo, Optical and electrical properties of ultra-thin indium tin oxide nanofilms on silicon for infrared photonics, Opt. Mater. Express 8 (2018) 1231, https://doi.org/10.1364/OME.8.001231.
[45] Y. Du, S. Liu, Z. Zhou, H.H. Lee, T.C. Ho, S.-P. Feng, C.Y. Tso, Study on the halide effect of $MA_4PbX_6{\cdot}2H_2O$ hybrid perovskites – from thermochromic properties to practical deployment for smart windows, Mater. Today Phys. 23 (2022) 100624, https://doi.org/10.1016/j.mtphys.2022.100624.
[46] Z. Liang, X. Liao, J. Yu, Z. Zhou, H. Wang, T. Zhang, C. Yi, L. Zhao, F. Chen, C. Wu, Long-term stability and efficiency of VO_2 nanostructure-based Thermochromic smart windows, ACS Appl. Nano Mater. 7 (2024) 21683–21691, https://doi.org/10.1021/acsanm.4c03595.
[47] Y. Chen, X. Zeng, J. Zhu, R. Li, H. Yao, X. Cao, S. Ji, P. Jin, High performance and enhanced durability of thermochromic films using VO_2 @ZnO core–shell nanoparticles, ACS Appl. Mater. Interfaces 9 (2017) 27784–27791, https://doi.org/10.1021/acsami.7b08889.
[48] B. Li, S. Tian, H. Tao, X. Zhao, Tungsten doped M-phase VO_2 mesoporous nanocrystals with enhanced comprehensive thermochromic properties for smart windows, Ceram. Int. 45 (2019) 4342–4350, https://doi.org/10.1016/j.ceramint.2018.11.109.
[49] N. Shen, S. Chen, R. Shi, S. Niu, A. Amini, C. Cheng, Phase transition hysteresis of tungsten doped VO_2 synergistically boosts the function of smart windows in ambient conditions, ACS Appl. Electron. Mater. 3 (2021) 3648–3656, https://doi.org/10.1021/acsaelm.1c00550.
[50] X. Chen, M. Wu, X. Liu, D. Wang, F. Liu, Y. Chen, F. Yi, W. Huang, S. Wang, Tuning the doping ratio and phase transition temperature of VO_2 thin film by dual-target co-sputtering, Nanomaterials 9 (2019) 834, https://doi.org/10.3390/nano9060834.
[51] M. Liu, X. Li, W. Zhang, L. Li, L. Li, C. Wang, G. Pei, B. Zhao, C. Zou, Three-state Thermochromic smart window for building energy-saving, Adv. Sci. 12 (2025), https://doi.org/10.1002/advs.202416688.